J. Fluid Mech. (2021), *vol*. 911, A25, doi:10.1017/jfm.2020.1003

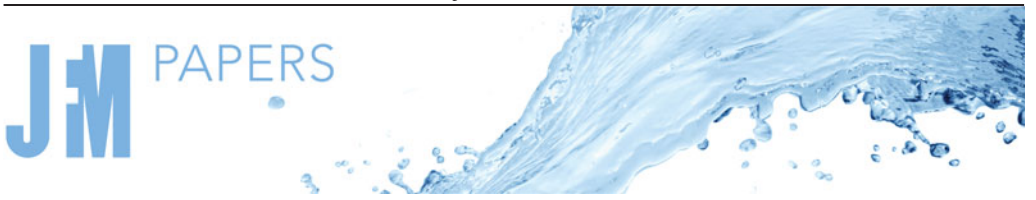

Helicity spectra and topological dynamics of vortex links at high Reynolds numbers

Demosthenes Kivotides[1],† **and Anthony Leonard**[2]

[1]Chemical Engineering, Strathclyde University, Glasgow G1 1XL, UK

[2]Aerospace, California Institute of Technology, Pasadena, CA 91125, USA

(Received 20 June 2020; revised 2 November 2020; accepted 4 November 2020)

We employ reconnection-capable, vortex filament methods and finite-volume, Navier–Stokes flow solvers to investigate the topological and helicity dynamics of vortex links for medium and high Reynolds numbers. Our vortex-dynamical model is based on discretization of vortex tubes into bundles of numerical analogues of vortex lines. Due to their nearly singular nature, the numerical vortex lines have topological writhe but not twist. By means of our reconnecting vortex tube model, it is shown that the helicity of a vortex link is conserved during the unknotting process. The dynamics of linking and writhe topological measures indicate that most of the initial linking becomes writhe during the post-reconnection evolution. The helicity spectra of the vortex link present alternating-sign helicity fluctuations at all (potential flow) scales up to the vortex core. At pre-reconnection times, these fluctuations are damped by Biot–Savart vortex stretching and helicity becomes single signed. The post-reconnection spectra indicate an inverse helicity cascade corresponding to the creation of a homogenized vortex blob, a process reminiscent of coherent structure formation in turbulence. An accompanying Navier–Stokes calculation of vortex link dynamics at Reynolds numbers $Re = 1500$ confirms the post-reconnection transformation of linking into different topological measures, the pre-reconnection damping of helicity spectra fluctuations and the spectral shift to low wavenumbers at post-reconnection times. Due to viscous dissipation action, however, this shift is accompanied by progressive reduction of helicity peak values.

Key words: vortex flows, turbulent flows

1. Introduction

Physics is often formulated in terms of conservation laws which, according to Noether's theorem, correspond to symmetries of key variables and their dynamical equations under

† Email address for correspondence: demosthenes.kivotides@strath.ac.uk

corresponding transformations (Schwichtenberg 2017). Fluid dynamics, in particular, is based on conservation laws for mass, energy and momentum that result from invariance of theoretical predictions under arbitrary system translations in space and time. In the case of inviscid, incompressible fluids, there are additional conservation laws that emanate from the fluid–particle relabelling symmetry (Padhye & Morrison 1996; Kambe 2007; Fukumoto 2008; Araki 2015, 2018; Kedia *et al.* 2018). This symmetry entails that, in the field-theoretic picture, the Eulerian flow velocity $\boldsymbol{u}(\boldsymbol{x}, t)$ remains invariant when, in the corresponding material or Lagrangian picture, the initial-time fluid–particle coordinate parametrization is arbitrarily changed. This leads to the global invariance of the inner product of velocity with frozen in the flow vector fields (Fukumoto 2008), whose initial values could be identified with the above mentioned arbitrary change of fluid–particle labels. In magnetohydrodynamics, the frozen field is the magnetic field and the corresponding invariant quantity is the cross helicity. In Eulerian fluid mechanics, the frozen field is the vorticity field $\boldsymbol{\omega}(\boldsymbol{x}, t)$, and the corresponding invariant quantity is the kinetic helicity density $h(\boldsymbol{x}, t) = \boldsymbol{u} \cdot \boldsymbol{\omega}$.

It is because vorticity is frozen in inviscid flow, and it is a local measure of solid-body-type rotation in the fluid, that the particle relabelling symmetry results in a valuable insight into flow structure: by projecting vorticity on the direction of velocity, and assuming, for example, a right-handed frame of reference, helicity indicates local right- ($h > 0$) or left-handedness ($h < 0$) of the local streamline screw whose helical axis coincides with the direction of velocity. So, assuming negligible viscous effects, the total measure of handedness or lack of reflection symmetry in the flow is conserved. This is an intriguing property of the Euler equations, whose effects on flow structure are much more subtle than those of conservation of momentum or energy. Notably, sometimes helicity is thought equivalent to chirality, but this can cause confusion, since, in physical mathematics (Schwichtenberg 2017), chirality is an intrinsic, relativistic, particle property which, in opposition to helicity, does not depend on the reference frame; hence, a particle has invariably the same chirality, although, depending on its state of motion and reference frame choice, can have either left- or right-handed helicity. In other words, by depending on the velocity field (rather than solely on its gradients), helicity fails to be locally Galilean invariant. This implies that, helicity-based, local flow analyses are dependent on reference frame choice.

Certainly, in the vast majority of flow phenomena, viscous effects are important, and the total kinetic helicity $\mathcal{H} = \int_{\mathcal{V}} \boldsymbol{u}(\boldsymbol{x}) \cdot \boldsymbol{\omega}(\boldsymbol{x})\, \mathrm{d}\boldsymbol{x}$, where $\mathcal{V}$ is the system's volume, is not a flow invariant. An example of such a flow is the dissipative dynamics of two vortex rings in the Hopf link configuration (Aref & Zawadski 1991; Brady, Leonard & Pullin 1998; Kivotides & Leonard 2003*a*). Initially, the vortex lines within the tubes are unlinked and untwisted. Although the flow outside the tube cores is essentially inviscid, the link is destroyed and topology changes via a dissipative vortex reconnection. Moffatt (1969, 2014) and Ricca & Moffatt (1992) indicated that this topological change is directly related to helicity, by deriving an intriguing relation between $\mathcal{H}$, a physical quantity, and topological measures of a system of N vortex tubes:

$$\mathcal{H} = \sum_{i \neq j} \Gamma_i \Gamma_j Lk_{ij} + \sum_i {\Gamma_i}^2 (Wr_i + Tw_i), \tag{1.1}$$

where Γ_i is the circulation of tube i, Lk_{ij} is the Gauss linking number of tubes i and j, and Wr_i and Tw_i are, correspondingly, the writhe and twist of tube i. The sum of Wr_i and Tw_i is the Călugăreanu self-linking number SLk_i, which measures the degree of knottedness of

single closed tubes, and, according to Călugăreanu's theorem (Călugăreanu 1961; Moffatt & Ricca 1992), is a topological invariant. Helpful discussions of these topological concepts in the contexts of physics applications are available in Scheeler *et al.* (2017) and Berger & Prior (2006). Remarkably, the formula relates helicity with linking measures, which are directly connected with curve geometry (§ 4 in this paper). This is because helicity is a measure of streamline right- or left-handedness, and this is exactly what the *Lk* number measures in a geometry, since for a system of i curves, $Lk = \sum_i w_i/2$, i.e. *Lk* is a summation over weights of all crossings between different curves. The crossings are counted on a two-dimensional projection of the curve system along an arbitrary direction, and their weights are $w = +1$ for each right-handed crossing and $w = -1$ for each left-handed crossing. On the helicity side, the counting becomes an integral, and the weights are automatically encoded in the signs of the inner products between velocity and vorticity. The circulation factors in the Moffatt & Ricca formula are then a dimensional book-keeping, as implied by the Biot–Savart law. Recently, new important developments indicated derivation of the skein relations of the HOMFLYPT polynomial for ideal fluid knots from helicity (Liu & Ricca 2015). Similar associations of helicity with other knot polynomials (Sossinsky 2004) or Vassiliev invariants above the lowest order (Mostovoy, Chmutov & Duzhin 2017) are highly desirable. It would certainly be important to find new conserved flow quantities that correspond to these types of invariants.

The Moffatt & Ricca formula offers new points of view for physics investigations. Indeed, let us consider, without loss of generality, a case where the ring cores (that set the characteristic scale of reconnection area, hence, also of dissipative effects) are much smaller than the ring diameters. Since the latter plausibly indicate the scale where most of net helicity ought to reside, one argues that, at sufficiently high Reynolds numbers, and correspondingly small reconnection durations, a small-scale dissipative effect (reconnection) ought not to alter significantly a large-scale quantity (helicity). To transfer intuition from turbulence physics, Taylor-scale dissipative processes destroy, at any time, a small part of the kinetic energy of the large, energy-containing motions. Such arguments would suggest that, at high Reynolds number ($Re \gg 1$), for helicity to be approximately the same before and after reconnection, the Moffatt & Ricca formula needs to predict a change of helicity from one type of topological measure (Lk_{ij}) to another ($Wr_i + Tw_i$). A topological justification of the same conclusion was offered by Pfister & Gekelman (1990). Employing ribbons for theoretical illustration, they argued that *Lk* becomes *Tw* during reconnection. We show here that, in our vortex-dynamical model, *Lk* becomes *Wr*, which is something similar, since Pfister & Gekelman (1990) and Moffatt & Ricca (1992) indicate how twist (formed by helical winding of one ribbon edge about the other) can be transformed to writhe (corresponding to self-intersections of the ribbon centreline in a two-dimensional projection of it) via continuous transformations. This interchangeability of *Wr* and *Tw* is implied by the topological nature of *SLk*, and can even be realized when topological calculations that refer to the same geometry employ different view angles (Klenin & Langowski 2000).

These matters were first experimentally clarified by Scheeler *et al.* (2014), who measured the post-reconnection *Wr* and showed that it was comparable with the initial *Lk* value. Their experimental techniques did not allow them to measure directly the post-reconnection twist, but the measured writhe values were adequate for demonstrating the relatively small effect of the reconnection on helicity levels. There are two important remarks implied by their results: (*a*) small helicity changes can correspond to marked changes in topological measures, i.e. for similar pre- and post-reconnection helicity levels, all initial linking becomes writhe and twist, and (*b*) in the spirit of the physical arguments

above, Re must be high. Indeed, $Re \sim 2 \times 10^4$ in the experiment of Scheeler *et al.* (2014). At sufficiently small Re, the link dynamics would tend to create writhe and twist, but, in the absence of adequately large inertia, the latter is overwhelmingly damped by viscosity, a process providing a topological interpretation of helicity dissipation.

The purpose of this work is to theoretically probe the high-Re helicity and topological dynamics of vortex links. There are three key aspects of our contribution. (*a*) We employ a discrete, yet finite-core, vortex-dynamical model of Hopf links, which corresponds to the limit of high-Reynolds-number vortex dynamics. In this respect, we took advantage of methods originating in quantum fluid dynamics (Kivotides 2018*b*; Galantucci *et al.* 2019), but adapted to Navier–Stokes vortex dynamics (Kivotides & Leonard 2003*a*), and successfully applied to high-Reynolds-number turbulence (Kivotides & Leonard 2004*a*,*b*, 2003*b*), magnetohydrodynamics (Kivotides, Mee & Barenghi 2007*b*) and solid–fluid dynamics (Kivotides *et al.* 2007*a*). These references include, among others, comparisons between quantum and classical vortex dynamics, details about the reconnection algorithm and the effects on performance of its various parameters, systematic comparison with numerical solutions of the Navier–Stokes equations, reproduction of key Navier–Stokes turbulence spectra scalings, turbulence kinematics and geometrical physics, as well predictions of kinematic magnetohydrodynamic dynamo spectra and depictions of particle–vortex interactions in turbulent suspensions. Our reconnection algorithm originates in the work of Schwarz on quantum vortex dynamics Schwarz (1985). However, there are important differences between quantum and classical vortex dynamics. The former case deals with discrete vortex lines of singular vorticity and constant (in all flow cases) circulations, whilst the second involves finite, dynamic core tubes with continuous vorticity distributions and freely varying circulations. During tube reconnection, many vortex lines (which discretize the tube vorticity) can reconnect in close succession. It is important to preserve tube integrity during this process. This requires a careful choice of the vortex approach distance upon which topological surgery takes place. In the calculations presented here, we have chosen the smallest distance that does not lead to unphysical results during tube stretching dynamics, as are erroneous Lk increments before the onset of reconnections. To be more specific, there is a different approach to reconnections in the two cases: in quantum fluids, reconnections are performed when two vortices approach closer than a computational reconnection distance (CRD) which is of the order of their numerical discretization length. Small CRD changes do not lead to large changes in the results. This is because, in quantum fluids, there are no finite-core vortex tubes, but only isolated line vortices (known as topological defects in quantum field theory). In classical fluids, however, CRD choice follows a more elaborate, iterative procedure. For the particular vortex core and circulation in the initial conditions, we start by employing a CRD of the order of the numerical discretization along the vortex contours, and we perform a series of computations with decreasing CRD. The main concerns are to keep tube integrity during reconnection, and, at the same time, not to have unphysical topological changes before reconnection onset. The final CRD chosen is the smallest CRD that satisfies both both of the above requirements. The details of the corresponding series of numerical calculations and their accompanying CRD values are discussed in the computational methodology section. Moreover, in the present context, we also apply the model of Kivotides & Leonard (2003*a*) with constant cores, i.e. without diffusive core growth; hence the sole physical effect of reconnections is to effect topological change. In this way, our vortices are numerical analogues of reconnecting, vortex lines in the high-Reynolds-number limit. (*b*) In contrast with the standard spectra of velocity or vorticity vector fields which refer to the squares (energy and enstrophy) of these quantities,

we employ methods for the computation of the spectra of the actual helicity values. Hence, our helicity spectra inform not only about the scale-by-scale partition of helicity, but also about the sign of the latter. Employing these methods, we accurately probe the interscale helicity transfer processes. (*c*) We calculate the topological measures in the Moffatt & Ricca formula with great precision, by transferring to vortex dynamics robust topology measuring methods first developed in the context of DNA biopolymer studies. After discussing the mathematical details of each of these tools, we apply them to vortex-link dynamics and discuss the resulting physics.

2. Discrete model of reconnecting vortex tubes

In order to theoretically match the high Reynolds numbers in experiments, and, in fact, to do even better in this respect, we note that in the limit of $Re \gg 1$ vortex-link dynamics, one expects a small (in comparison with the total energy content) amount of dissipation, whose main role is to facilitate vortex reconnection. These physical requirements are matched by the mesoscopic model of quantum vortex dynamics employed in superfluids research (Kivotides 2018*b*, 2014). Whilst at microscopic scales an (inviscid) supefluid flows under the influence of its quantum stress that controls fluid density and effects reconnections (Legget 2006), at mesoscopic scales a superfluid behaves like an incompressible fluid with phenomenological reconnections (Feynman 1955; Schwarz 1985; Kivotides 2014). In this context, the vortices are slender filaments, and vorticity is distributed within their finite cores via suitable smoothing kernels:

$$\boldsymbol{\omega}(\boldsymbol{x}) = \sum_i \Gamma_i \int_{\mathcal{C}_i} \frac{p(|\boldsymbol{x} - \boldsymbol{r}_i(\xi)|/\sigma)}{\sigma^3} \frac{\partial \boldsymbol{r}_i(\xi)}{\partial \xi} \, \mathrm{d}\xi, \tag{2.1}$$

where the circulation of tube i is Γ_i and its centreline $\mathcal{C}_i$ is given by the space curve $\boldsymbol{r}_i(\xi)$, where ξ is the arclength parametrization of curve $\mathcal{C}_i$. The function p determines the vorticity distribution over the core of the tube having an effective radius of σ, and facilitates stable numerical calculations. The calculations are performed with the Gaussian kernel of Winckelmans & Leonard (1993):

$$p\left(\frac{r}{\sigma}\right) = \frac{1}{(2\pi)^{3/2}} \mathrm{e}^{-r^2/(2\sigma^2)}. \tag{2.2}$$

Inserting the above definition of vorticity in the Biot–Savart integral reduces the latter to a sum of line integrals over each filament centreline contour:

$$\boldsymbol{u}(\boldsymbol{x}) = -\sum_i \frac{\Gamma_i}{4\pi} \int_{\mathcal{C}_i} \mathrm{d}\xi \frac{Q(\phi)}{(\sqrt{2}\sigma)^3} \frac{\partial \boldsymbol{r}_i(\xi)}{\partial \xi} \times (\boldsymbol{r}_i(\xi) - \boldsymbol{x}), \tag{2.3}$$

where function $Q(\phi)$ (with $\phi = |\boldsymbol{r}_i - \boldsymbol{x}|/\sqrt{2}\sigma$) depends on the particular smoothing kernel employed. For the Gaussian kernel case, it is (Leonard 1985; Winckelmans & Leonard 1993)

$$Q(\phi) = \frac{\mathrm{erf}(\phi/\sqrt{2}) - \sqrt{\dfrac{2}{\pi}}\phi \mathrm{e}^{-\phi^2/2}}{\phi^3}, \quad \boldsymbol{r}_i(\xi) \neq \boldsymbol{x}, \tag{2.4}$$

$$Q(\phi) = \sqrt{\frac{2}{9\pi}}, \quad \boldsymbol{r}_i(\xi) = \boldsymbol{x}. \tag{2.5}$$

There are some important features: by employing the smoothing kernel, we transform line vortices to vortex tubes. This is very much in agreement with the derivation of the Moffatt & Ricca formula (Moffatt & Ricca 1992) where both writhe and twist are forms of self-linking involving the vortex lines within single tubes. Pfister & Gekelman (1990), Moffatt & Ricca (1992) and Scheeler *et al.* (2014) offer nice illustrations of this point. Hence, our model entails both *Lk* and *Wr* physics. On the other hand, since the numerical tubes are not capable of core deformation, by default, there is no *Tw* in our flow field.

It is important to discuss this last point to accurately embed our method within the general context of topological vortex physics. In the context of single vortex tube dynamics, there are two relevant topological quantities: *Wr* and *Tw* (Asgari-Targhi & Berger 2009). They measure the topology of the continuum bundle of vortex lines that comprise the tube, with each line providing infinitesimal contribution to the total flux. So in continuum physics, we need an infinity of vortex lines to model each of the two finite tubes that comprise a Hopf link. In our numerical approach, we discretize the finite-core tubes into bundles of finite number of vortices. The cores of the latter are (by construction) non-deformable, and do not include twisted vortex lines. In other words, there are no physically dynamical cores associated with our discrete vortices, whose evolution we can meaningfully track in time. At every time step, the line vortices are 'dressed' with (constant) numerical cores, which, once the smoothed velocity field is computed, are discarded, and do not propagate to the next time step. As mentioned above, this smoothing includes *Wr* physics but not *Tw* physics. Our results are physically consistent, since, further on, we demonstrate an excellent correspondence between topological measures based on the discrete vortices (excluding *Tw*) and flow field helicity values. Attributing *Tw* to our discrete vortices would add to topology a feature that is not present in the flow field. This would, by default, invalidate our computation, since the helicity spectra, for example, would not correspond to the topological helicity values.

Certainly, by defining an effective core based on the boundaries of numerical vortex bundles, one can compute *Tw* values for the macroscopic tubes, and, by considering the contour of the bundle-centreline vortex, also *Wr* values, if needed. It is only the *Tw* of the discrete vortices that is not modelled within the numerical approximation. So let us discuss in detail how our numerical method tackles vortex-dynamical processes that involve *Tw* dynamics. Take for example (Asgari-Targhi & Berger 2009) the case of a circular vortex tube that is given a large-scale turn so that it approaches a figure-of-eight shape. Since there is a variation of *Wr*, helicity conservation implies an opposite sign variation of *Tw*. Such a situation is handled in our method by discretizing the original tube into a bundle of elementary (*Tw*-free) vortices. During the figure-of-eight formation, the vortices in the tube get twisted generating *Tw* in the macroscopic tube, whilst the computation of the macroscopic tube *Wr* is based on the vortex at the bundle centreline. On the other hand, by decreasing the circulation of discrete vortices and the discretization length along vortex contours, we can increase the accuracy and resolution of our calculations as desired.

On another front, the phenomenological (jump process) nature of the reconnections in our system (Kivotides 2014) is fully compatible with the discrete character of topological change, and, indeed, Pfister & Gekelman (1990) employ a similar jump process in their demonstration of helicity conservation during ribbon reconnection. In conclusion, we expect that, due to lack of dissipation, and within the accuracy levels of our vortex-dynamics methodology, helicity is going to be conserved, modulo transient, spurious physical effects due to the discontinuous nature of reconnections in our model, yet the topological dynamics will be accurate, and helicity-related conclusions qualitatively

correct. On the other hand, we gain important insight into high-Reynolds-number vortex dynamics.

To cross-check our calculations, we compute helicity with both vortex dynamics and topological formulae. Within the former (Winckelmans & Leonard 1993), total vorticity $\mathcal{H}$ is given by

$$\mathcal{H} = \sum_{i,j} \Gamma_i \Gamma_j \iint \frac{q_\sigma(\boldsymbol{r}_i - \boldsymbol{r}_j)}{|\boldsymbol{r}_i - \boldsymbol{r}_j|} \left[(\boldsymbol{r}_i - \boldsymbol{r}_j) \cdot \left(\frac{\partial \boldsymbol{r}_i(\xi)}{\partial \xi} \times \frac{\partial \boldsymbol{r}_j(\xi')}{\partial \xi'} \right) \right] \mathrm{d}\xi \, \mathrm{d}\xi', \tag{2.6}$$

where $q_\sigma(\boldsymbol{r}) = q(|\boldsymbol{r}|/\sigma)$ and

$$q(\rho) = \int_0^\rho p(t) t^2 \, \mathrm{d}t. \tag{2.7}$$

In discretizing actual Navier–Stokes vortex tubes in terms of elementary vortex filaments, we employ the methods of Knio & Ghoniem (1990) and Winckelmans & Leonard (1993). Although our approach follows closely that of Winckelmans & Leonard (1993), the presence of reconnections in our model imposes strict discretization constraints, not present in previous works. To set up a discretization of a ring-like vortex tube, we choose the 'quantum' of circulation, i.e. the circulation Γ_i of each elementary vortex i, which is set equal to κ for all vortices, and the circulation Γ_m of the 'macroscopic' tube. The ratio $n_v = \Gamma_m/\kappa$ can be thought of as the number of 'grid points' that are required to approximate the internal dynamics of the macroscopic vortex tube. The idea in Knio & Ghoniem (1990) and Winckelmans & Leonard (1993) is to discretize the macroscopic tube into a sequence of n_c layers (toroidal shells), each one containing $8n_c$ elementary vortices. Hence, n_v determines the number of discretization layers. By taking the outer radius of each layer (measured from the tube centreline and on a plane normal to the latter) equal to $(2n_c + 1)r_\ell$, and having the elementary vortices passing through each layer along a perimeter of radius $r_c = (1 + 12n_c^2/6n_c)r_\ell$ (also measured from the tube centreline), we place each vortex at the centre of an area $\pi r_\ell^2 = \pi R_t^2/n_v$. Here, R_t is the tube core radius. Notably, in this construction, the macroscopic tube centreline is always occupied by a line vortex. A central point is that, in the phenomenological reconnections model, the elementary vortices reconnect when they approach closer than $\delta \approx 0.1\Delta\xi$, where $\Delta\xi$ is the discretization length along the vortices. We need the vortices to reconnect as a result of vortex-dynamically generated configurations, and not artificially, due to small distances from each other in the initial conditions. Hence, $\delta = 0.1\Delta\xi$ must be significantly smaller than r_ℓ (in the calculations it is smaller by a factor of 4), and this imposes a lower resolution limit that, in turn, determines computational complexity levels. Computational complexity scales with the N^2 operations required by Biot–Savart interactions (where N is the number of numerical vortex segments). To double the Reynolds number, we need to double the bundle circulation, hence also double the number of line vortices in the system. Keeping resolution the same, the number of vortex segments becomes, in this way, $2N$, and thus the computational complexity increases by a factor of 4.

3. Helicity spectra for Navier–Stokes and vortex-dynamical formulations

3.1. *Navier–Stokes spectra*

We aim to derive here a formula for the spectrum of helicity (rather than its square). We first consider the field theoretic case, before the vortex-dynamics one. The total helicity $\mathcal{H}$

is given by

$$\mathcal{H} = \int \boldsymbol{u}(\boldsymbol{x}) \cdot \boldsymbol{\omega}(\boldsymbol{x}) \, \mathrm{d}\boldsymbol{x}. \tag{3.1}$$

Substituting $\boldsymbol{u}$ and $\boldsymbol{\omega}$ with their inverse Fourier transforms (we use $1/2\pi$ and $\exp(-\mathrm{i}\boldsymbol{k}\cdot\boldsymbol{x})$ factors when taking the inverse transform, and we define $k = 2\pi/\ell$, with ℓ a length scale) we have

$$\mathcal{H} = \left(\frac{1}{2\pi}\right)^6 \iiint \hat{\boldsymbol{u}}(\boldsymbol{k}) \cdot \hat{\boldsymbol{\omega}}(\boldsymbol{k}') \exp\left(-\mathrm{i}\boldsymbol{k}\cdot\boldsymbol{x} - \mathrm{i}\boldsymbol{k}'\cdot\boldsymbol{x}\right) \mathrm{d}\boldsymbol{x}\,\mathrm{d}\boldsymbol{k}\,\mathrm{d}\boldsymbol{k}'. \tag{3.2}$$

Integration over $\boldsymbol{x}$ produces the delta function $(2\pi)^3\delta(\boldsymbol{k}+\boldsymbol{k}')$. In addition, we have that

$$\hat{\boldsymbol{u}}(\boldsymbol{k}) = -\frac{\mathrm{i}\boldsymbol{k}\times\hat{\boldsymbol{\omega}}(\boldsymbol{k})}{k^2}, \tag{3.3}$$

and therefore (3.3) becomes

$$\mathcal{H} = -\frac{\mathrm{i}}{(2\pi)^3}\int \frac{\boldsymbol{k}\cdot\left[\hat{\boldsymbol{\omega}}(\boldsymbol{k})\times\hat{\boldsymbol{\omega}}(-\boldsymbol{k})\right]}{k^2}\,\mathrm{d}\boldsymbol{k}. \tag{3.4}$$

Using spherical coordinates in $\boldsymbol{k}$-space, i.e. $\mathrm{d}\boldsymbol{k} = \mathrm{d}\boldsymbol{\Omega}_k k^2\,\mathrm{d}k$ and transforming back to real space, (3.4) becomes

$$\mathcal{H} = -\frac{\mathrm{i}}{(2\pi)^3}\iiint\left(\int \boldsymbol{k}\cdot\left[\boldsymbol{\omega}(\boldsymbol{x})\times\boldsymbol{\omega}(\boldsymbol{x}')\right]\exp\left(\mathrm{i}\boldsymbol{k}\cdot(\boldsymbol{x}-\boldsymbol{x}')\right)\right)\mathrm{d}\boldsymbol{\Omega}_k\,\mathrm{d}\boldsymbol{x}\,\mathrm{d}\boldsymbol{x}'\,\mathrm{d}k. \tag{3.5}$$

Integration over $\boldsymbol{\Omega}_k$ is accomplished simply by assuming $\boldsymbol{x}-\boldsymbol{x}'$ is in the polar direction so that

$$\mathcal{H} = -\frac{\mathrm{i}}{(2\pi)^2}\iiint\left(\int_{-1}^{1} k\mu\frac{\boldsymbol{x}-\boldsymbol{x}'}{|\boldsymbol{x}-\boldsymbol{x}'|}\cdot\left[\boldsymbol{\omega}(\boldsymbol{x})\times\boldsymbol{\omega}(\boldsymbol{x}')\right]\exp\left(\mathrm{i}k\mu|\boldsymbol{x}-\boldsymbol{x}'|\right)\mathrm{d}\mu\right)\mathrm{d}\boldsymbol{x}\,\mathrm{d}\boldsymbol{x}'\,\mathrm{d}k, \tag{3.6}$$

where μ is the cosine of the angle between $\boldsymbol{k}$ and $\boldsymbol{x}-\boldsymbol{x}'$. Integration over μ in (3.6) gives

$$\mathcal{H} = -\frac{1}{2\pi^2}\int_k\iint k\frac{\mathrm{d}}{\mathrm{d}k}\left(\frac{\sin(k|\boldsymbol{x}-\boldsymbol{x}'|)}{k|\boldsymbol{x}-\boldsymbol{x}'|}\right)\frac{\boldsymbol{x}-\boldsymbol{x}'}{|\boldsymbol{x}-\boldsymbol{x}'|^2}\cdot\left[\boldsymbol{\omega}(\boldsymbol{x})\times\boldsymbol{\omega}(\boldsymbol{x}')\right]\mathrm{d}\boldsymbol{x}\,\mathrm{d}\boldsymbol{x}'\,\mathrm{d}k. \tag{3.7}$$

Thus we can define the helicity spectrum $\hat{\mathcal{H}}(k)$ as

$$\hat{\mathcal{H}}(k) = -\frac{1}{2\pi^2}\iint k\frac{\mathrm{d}}{\mathrm{d}k}\left(\frac{\sin(k|\boldsymbol{x}-\boldsymbol{x}'|)}{k|\boldsymbol{x}-\boldsymbol{x}'|}\right)\frac{\boldsymbol{x}-\boldsymbol{x}'}{|\boldsymbol{x}-\boldsymbol{x}'|^2}\cdot\left[\boldsymbol{\omega}(\boldsymbol{x})\times\boldsymbol{\omega}(\boldsymbol{x}')\right]\mathrm{d}\boldsymbol{x}\,\mathrm{d}\boldsymbol{x}', \tag{3.8}$$

so that

$$\mathcal{H} = \int_0^\infty \hat{\mathcal{H}}(k)\,\mathrm{d}k. \tag{3.9}$$

Indeed integration of $\hat{\mathcal{H}}(k)$ gives

$$\mathcal{H} = \frac{1}{4\pi}\iint\frac{\boldsymbol{x}-\boldsymbol{x}'}{|\boldsymbol{x}-\boldsymbol{x}'|^3}\cdot\left[\boldsymbol{\omega}(\boldsymbol{x})\times\boldsymbol{\omega}(\boldsymbol{x}')\right]\mathrm{d}\boldsymbol{x}\,\mathrm{d}\boldsymbol{x}'. \tag{3.10}$$

3.2. *Vortex-dynamics spectra*

The helicity spectrum formula for the vortex-dynamical model is

$$\hat{\mathcal{H}} = -\frac{\hat{p}^2(k\sigma)}{2\pi^2}\sum_{i,j}\Gamma_i\Gamma_j\iint k\frac{\mathrm{d}}{\mathrm{d}k}\left(\frac{\sin(k|\boldsymbol{r}_i(\xi)-\boldsymbol{r}_j(\xi')|}{k|\boldsymbol{r}_i(\xi)-\boldsymbol{r}_j(\xi')|}\right)\frac{\boldsymbol{r}_i(\xi)-\boldsymbol{r}_j(\xi')}{|\boldsymbol{r}_i(\xi)-\boldsymbol{r}_j(\xi')|^2} \cdot\left[\frac{\partial\boldsymbol{r}_i(\xi)}{\partial\xi}\times\frac{\partial\boldsymbol{r}_j(\xi')}{\partial\xi'}\right]\mathrm{d}\xi\,\mathrm{d}\xi', \tag{3.11}$$

where the function $\hat{p}$ corresponding to the employed Gaussian kernel is $\hat{p}(k\sigma) = \mathrm{e}^{-(k\sigma)^2/2}$. Note that $\hat{p}(0) = 1$. Both formulae have an apparent singularity when considering the self-contribution to helicity of a field or vortex point. However, by calculating analytically the derivative in (3.12)

$$k\frac{\mathrm{d}}{\mathrm{d}k}\left(\frac{\sin(k|\boldsymbol{r}_i(\xi)-\boldsymbol{r}_j(\xi')|}{k|\boldsymbol{r}_i(\xi)-\boldsymbol{r}_j(\xi')|}\right) = \cos(k|\boldsymbol{r}_i(\xi)-\boldsymbol{r}_j(\xi')|) - \frac{\sin(k|\boldsymbol{r}_i(\xi)-\boldsymbol{r}_j(\xi')|)}{k|\boldsymbol{r}_i(\xi)-\boldsymbol{r}_j(\xi')|}, \tag{3.12}$$

employing L'Hŏpital's rule to compute the limit $\sin x/x$ when $x \to 0$ and expanding the cross-product $\partial\boldsymbol{r}_i(\xi)/\partial\xi \times \partial\boldsymbol{r}_j(\xi')/\partial\xi'$ around ξ when $\xi' \to \xi$, one can easily deduce that the self-contributions are equal to zero.

For an alternative derivation of the helicity spectrum based on two-point correlation functions and applied to magnetohydrodynamic dynamo physics, see Asgari-Targhi & Berger (2009).

4. Methods for calculating linking and writhe

To compute topological dynamics, we only need calculate *Lk* and *Wr*, since, as mentioned above, *Tw* in the Moffatt & Ricca formula is zero by default in our vortex dynamics. For completeness, we discuss, however, how *Tw* has been taken into account in other vortex-dynamics studies (Zuccher & Ricca 2015, 2017; Hänninen, Hietale & Salman 2016). Hänninen *et al.* (2016) study *Tw* by constructing macroscopic tubes from single quantum vortices, which are bundled together and endowed with Kelvin wave excitations that are mild enough to allow the tubes to remain coherent for finite period of time. By considering a ribbon based on the centreline of such macroscopic tubes, *Tw* can be meaningfully defined and measured. However, this approach is meaningful only as long as the tube remains coherent. Our macroscopic tubes undergo reconnections and other non-trivial dynamics that do not preserve tube coherence. Hence, by basing our topological analysis on *Lk* and *Wr* of elementary vortices, we perform a more general analysis that does not rely on assumptions of tube integrity. On the other hand, the works of Zuccher & Ricca (2015, 2017) and Kedia *et al.* (2018) indicate that *Tw* can meaningfully be ascribed to a discrete quantum vortex, but this refers to core dynamics governed by quantum stresses active at microscopic scales, and are not relevant to mesoscopic scales or to classical vortex dynamics, where quantum stresses are absent. In other words, the *Tw* of Zuccher & Ricca (2015, 2017) and Kedia *et al.* (2018) is not relevant to classical fluid dynamics, and that of Hänninen *et al.* (2016) is entailed in the topology of the elementary vortex system.

We follow the method of Klenin & Langowski (2000), which was developed in the context of biopolymer studies, but can also be applied to vortex dynamics, by taking advantage of the discretization of each vortex into closed polygonal curves. Then, the total linking $Lk = \sum_i \sum_j Lk_{ij}$ is the sum of all linking numbers Lk_{ij} between possible vortex

pairs i and j, noting that $Lk_{ij} = Lk_{ji}$ and $Lk_{ii} \equiv 0$. Each specific linking number Lk_{ij} is given by

$$Lk_{ij} = \sum_{k=1}^{N_i} \sum_{l=1}^{N_j} \frac{\Omega_{kl}}{4\pi}, \tag{4.1}$$

where N_i and N_j are the number of discretization segments of vortices i and j, respectively. Here $\Omega_{kl}/4\pi$ is the Gauss integral along segments k and l, with k and l belonging to two different vortices. Integral Ω_{kl} is computed in terms of four vectors: $\boldsymbol{r_1}$ and $\boldsymbol{r_2}$ corresponding to start and end points of segment k, and $\boldsymbol{r_3}$ and $\boldsymbol{r_4}$ corresponding to start and end points of segment l. By using $\boldsymbol{r_{ij}} \equiv \boldsymbol{r_j} - \boldsymbol{r_i}$, we have

$$\Omega_{kl} = \Omega^*_{kl} \mathrm{sign}\left((\boldsymbol{r_{34}} \times \boldsymbol{r_{12}}) \cdot \boldsymbol{r_{13}}\right), \tag{4.2}$$

where

$$\Omega^*_{kl} = \arcsin\left(\boldsymbol{n_1} \cdot \boldsymbol{n_2}\right) + \arcsin\left(\boldsymbol{n_2} \cdot \boldsymbol{n_3}\right) + \arcsin\left(\boldsymbol{n_3} \cdot \boldsymbol{n_4}\right) + \arcsin\left(\boldsymbol{n_4} \cdot \boldsymbol{n_1}\right) \tag{4.3}$$

and

$$\boldsymbol{n_1} = \frac{\boldsymbol{r_{13}} \times \boldsymbol{r_{14}}}{|\boldsymbol{r_{13}} \times \boldsymbol{r_{14}}|}, \quad \boldsymbol{n_2} = \frac{\boldsymbol{r_{14}} \times \boldsymbol{r_{24}}}{|\boldsymbol{r_{14}} \times \boldsymbol{r_{24}}|}, \quad \boldsymbol{n_3} = \frac{\boldsymbol{r_{24}} \times \boldsymbol{r_{23}}}{|\boldsymbol{r_{24}} \times \boldsymbol{r_{23}}|}, \quad \boldsymbol{n_4} = \frac{\boldsymbol{r_{23}} \times \boldsymbol{r_{13}}}{|\boldsymbol{r_{23}} \times \boldsymbol{r_{13}}|}. \tag{4.4a–d}$$

The Wr_i of a single curve i is similarly computed:

$$Wr_i = 2 \sum_{k=2}^{N_i} \sum_{l<k} \frac{\Omega_{kl}}{4\pi}, \tag{4.5}$$

where relations $\Omega_{kl} = \Omega_{lk}$ and $\Omega_{k(k+1)} = \Omega_{kk} \equiv 0$ apply.

5. Topology and helicity in vortex link dynamics

5.1. *Vortex-dynamical calculation*

The initial conditions consist of two tubes in Hopf link configuration (figure 1*a*). To limit computational complexity, we have chosen $n_v = 9$. Based on tube centreline radius R_c and tube circulation Γ_m, we define a unit time $t_u = R_c^2/\Gamma_m$. Helicity values are normalized with κ^2, so that they can be directly compared with Wr or Lk values. The effective tube radius is $R_t = 0.2R_c$.Due to their Biot–Savart interactions, the tubes are stretched as they locally align with each other on the road to reconnection (figure 1*b*). The latter takes place discontinuouly, as a sequence of pair reconnections between elementary vortices belonging to different tubes (figure 1*b*,*c*). Once the stretched reconnection 'bridge' disappears (figure 1*d*), the system evolves into a blob of fluctuating vorticity (figure 1*e*,*f*), and by the time of $3.5t_u$, the initial configuration is no longer discernible. Due to the complexity of the vortex tangle comprising the resulting blob of vorticity, there is continuing reconnections activity between the elementary vortices.

To check the consistency between vortex dynamics and topology, we have computed helicity employing both its Moffatt & Ricca and vortex-dynamic (relation (3.11)) formulae. In all of following results, helicity values are normalized by dividing with appropriate Γ^2 factors, so that the initial helicity value of the vortex link is equal to two, in both vortex-dynamical and Navier–Stokes calculations. There is very good

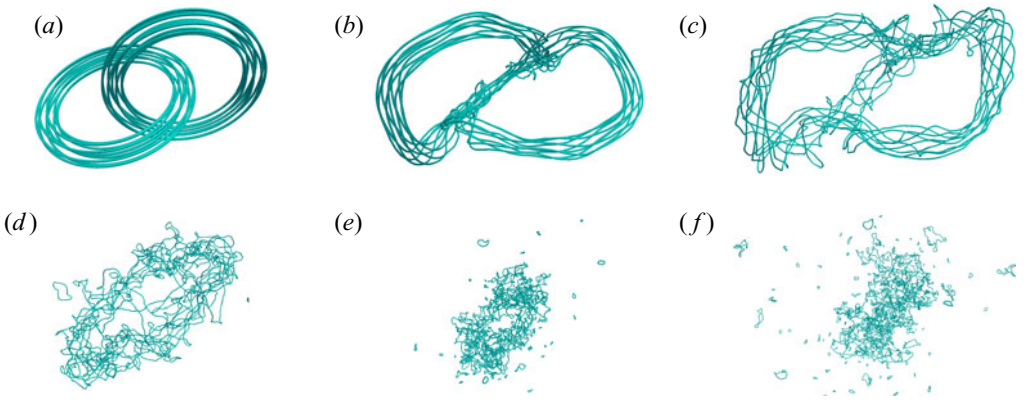

Figure 1. A vortex link made of discretized tubes reconnects and evolves into a blob of fluctuating vorticity. From (*a*) to (*f*) the times are: 0, 0.42, 0.56, 1.12, 2.24 and 3.5 (t_u units).

agreement (figure 2*a*) between the two sets of values, except close to the reconnection threshold, where vortex dynamics is not as accurate as topology. This difference between vortex-dynamical and topological evaluations is due to the fact that topological helicity evaluation does not depend on the geometry of the linked lines, and hence it is exact for all resolutions, which is not the case for the vortex-dynamical evaluation. Hence, in the latter case, results can only approximate the exact (topological) helicity in direct correspondence with the employed resolution. Taking into account that we have a link involving nine pairs of vortices, we expect $Lk = 162$ at $t = 0$, which is our topological result, which is matched exactly by the vortex-dynamical helicity value (figure 2*b*). As expected, Lk remains constant until the onset of reconnections. Since our vortex dynamics employs topological (i.e. cut and glue) reconnections (Pfister & Gekelman 1990), and vortex evolution obeys the Euler equations, there is no dissipation in our system (which is why we propose it as an appropriate model of high-Reynolds-number vortex dynamics). Hence, in the limit of very high resolution, when reconnections are pointwise and occur upon vortex contact, we expect helicity to be conserved, and this, indeed, is indicated by the results, after a transient of duration $\sim 0.5t_u$. This transient is an artifact of the discontinuous (jump process) nature of reconnections in our calculation. This, in turn, is a result of the relatively coarse grid that we employ in order to tame computational complexity. In an ideal computation, the employed fine grid would resolve all possible small-scale processes and vortices would reconnect upon quasi-contact. In such a calculation, the instantaneous drop of Lk upon reconnection would be fully compensated by an instantaneous rise of Wr. Our grid is not dense enough to capture this small-scale Wr, and hence it takes some time ($\sim 0.5t_u$) for Wr to attain its appropriate levels. To demonstrate this assertion, we zoomed in the reconnection zone of a link made of single vortices, employing a grid six times denser than the one employed in the vortex-bundle case. We found that, while the coarse grid gave post-reconnection Wr equal to approximately 27 % of pre-reconnection Lk, the dense grid increased this value to 66 %. Notably (figure 2*b*), the post-reconnection helicity is not all Wr, since there is reconnection-driven, continuous Lk formation/destruction activity. The corresponding reconnections are not related to the unlinking process, but take place within the emergent vortex blob. Their number depends on the employed reconnection criterion δ, i.e. the distance of approach between two filaments whereupon a reconnection jump is performed. We have tried different calculations with $\delta = [0.10, 0.15, 0.25, 0.50]\Delta\xi$. The corresponding helicity plateau values (i.e. after the transient induced by the reconnection

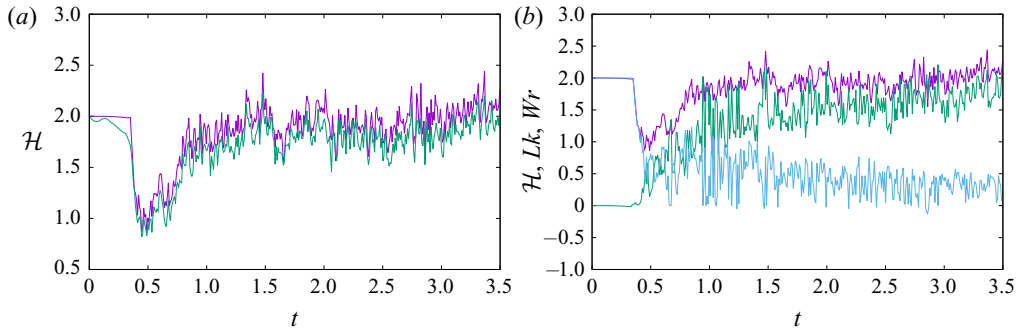

Figure 2. Vortex dynamics calculation. (*a*) Scaled helicity values obtained via the Moffatt & Ricca formula (upper curve) and directly from flow quantities (lower curve). (*b*) Scaled helicity values $\mathcal{H}$ obtained via the Moffatt & Ricca formula (upper curve), *Wr* (middle curve for post-reconnection times) and *Lk* (lower curve for post-reconnection times).

jumps has ceased) are $[1, 1.17, 1.31, 1.5]H_0$, where H_0 is the initial helicity value. The shown results correspond to the smallest physically acceptable δ. Smaller δ values lead to (unphysical) *Lk* value increments before the onset of reconnections, and larger δ values produce post-reconnection helicity levels that exceed the initial value. Hence, the smallest δ value producing physically acceptable reconnections implies also conservation of helicity. This is certainly an attractive feature of the model.

At this point, our findings agree with physical and topological intuitions, and available experimental results. Indeed, as indicated in Pfister & Gekelman (1990) and Scheeler *et al.* (2014), the initial *Lk* is mainly transformed into *Wr*, and the total helicity is conserved. To proceed further and understand better helicity structure, we look at helicity spectra $\hat{\mathcal{H}}(k)$. Remarkably, in a way reminiscent of energy spectra (Leonard 1985), the $\hat{\mathcal{H}}(k)$ of a link made of two single rings fluctuates between positive and negative values at all (resolvable) scales (figure 3*a*). We have checked that the integration of the spectra in wavenumber space gives exactly the total system helicity.When the link is made of vortex bundles instead of single vortices (figure 3*b*), there is a similar fluctuating behaviour at large scales, but the fluctuations die out fast. It can be concluded that the high k helicity fluctuations are the signature of the combined potential vortex flow field around elementary vortices. By creating bundles of the latter, we create macroscopic tubes with finite-diameter, solid-body rotating cores, which (by default) have zero helicity. Indeed, it was easy to check that the cut-off of the spectrum coincides with the effective core of the macroscopic tubes. The spectra indicate that, as expected, there is a net positive helicity at large scales, but this net amount is the sum of alternating-sign helicity contributions at progressively smaller scales. What happens to helicity spectra as a result of the reconnection? There are two distinctive dynamical regimes. The first corresponds to the road to reconnection (figure 4*a*). There, the initial spectrum fluctuations are damped, and as total helicity is conserved, there is an elimination of significant negative helicity values. Hence, although in the 'perfect' link of the initial conditions the positive net helicity is the small difference between positive and negative values, just before reconnection there is mostly positive helicity in the system. This could very well be the spectral signature of stretched, reconnection bridge formation (figure 1*b*). After unlinking, we have an inverse cascade of helicity from small to large scales (figure 4*b*). This is an intriguing feature that reverses the pre-reconnection tendency of large-scale helicity damping. It corresponds to the formation of the homogenized vortex

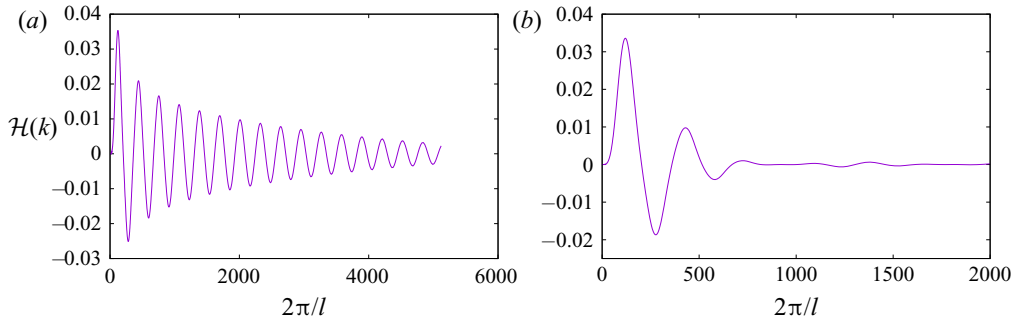

Figure 3. Vortex dynamics calculation. (*a*) Helicity spectra $\hat{\mathcal{H}}(k)$ for a link composed of single line vortices. (*b*) Helicity spectra $\hat{\mathcal{H}}(k)$ for a link of tubes made of bundles of nine line vortices each.

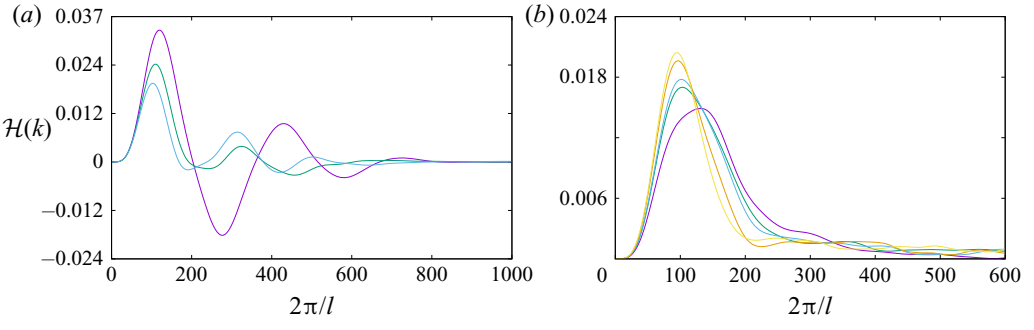

Figure 4. Vortex dynamics calculation. (*a*) Pre-reconnection helicity spectra $\hat{\mathcal{H}}(k)$ at times $t = 0$, $t = 0.2$ and $t = 0.28$ (t_u units). Smaller times correspond to curves with higher peaks at small wavenumbers. (*b*) Post-reconnection helicity spectra $\hat{\mathcal{H}}(k)$ at times $t = 1.02$, $t = 1.845$, $t = 2.02$, $t = 2.50$ and $t = 2.825$ (t_u units). Larger times correspond to curves with higher peaks at smaller wavenumbers. As a result of an inverse helicity cascade, a peak is formed at small wavenumbers.

blob, with helicity concentrated at the scale of the (effective) blob diameter. This inverse cascade process is directly connected to the conservation of helicity in an inviscid system.

The above considerations suggest the usefulness of helicity spectra in characterizing vortex-dynamical processes. On the other hand, we have checked that the observed rapid changes in the topological measures of helicity do not affect the shape of the spectrum. This is understood by considering that helicity is a flow quantity that requires significant global changes in flow patterns in order to have its spectrum altered. On the other hand, the topology can change on a much faster scale in a 'quantum' fashion. As indicated by the results, it is reasonable to expect that different topologies could correspond to the same spectra. In other words, although helicity is always indicative of the amount of handedness in the flow, and therefore of the linking topology, we cannot use the latter to characterize key flow processes as the above inverse cascade. For this purpose, more potent topological measures would be needed, as are, for example, the above mentioned knot polynomials and Vassiliev invariants above the lowest order.

5.2. *Navier–Stokes calculation*

Computational complexity forbids probing high-Reynolds-number flows with Navier–Stokes calculations. Overcoming this limitation was a key motive for developing

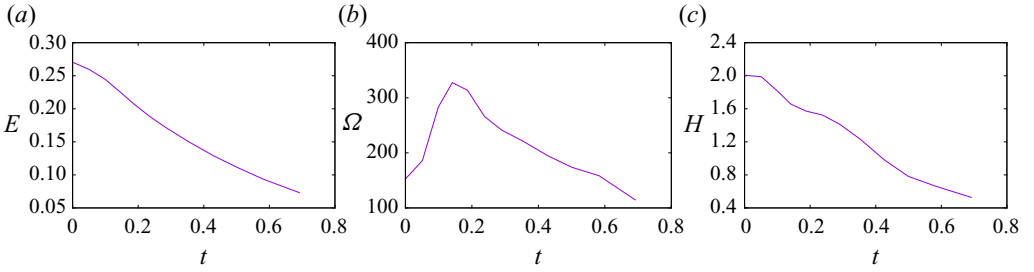

Figure 5. Navier–Stokes calculation. Vortex link at $Re = 1500$. (*a*) Scaled mean energy versus scaled time. (*b*) Scaled mean enstrophy versus scaled time. (*c*) Scaled total helicity versus scaled time.

the vortex-dynamical approach. In this respect, a 512^3 grid size was shown to provide adequate resolution for capturing vortex link dynamics at $Re = 1500$, where $Re = \Gamma/\nu$, Γ (which is analogous to Γ_m in the vortex-dynamical formulation) is the circulation of each vortex tube and ν is the viscosity of the fluid. The numerical method is a projection, finite-volume technique which is described in detail elsewhere (Kivotides 2018*b*). The boundary conditions are periodic. To ensure that viscous dissipation processes are adequately captured, the calculation resolves their characteristic time scale $t_u = R_t^2/\nu$, where R_t is the tube-core radius, which is equal to $0.2R_c$, and R_c is the tube-centreline radius. Time is scaled with t_u, total helicity $\mathcal{H} = \int_{\mathcal{V}} \boldsymbol{u}(\boldsymbol{x}) \cdot \boldsymbol{\omega}(\boldsymbol{x})\, \mathrm{d}\boldsymbol{x}$ with Γ^2, mean enstrophy $\Omega = (0.5/\mathcal{V}) \int_{\mathcal{V}} \boldsymbol{\omega}(\boldsymbol{x}) \cdot \boldsymbol{\omega}(\boldsymbol{x})\, \mathrm{d}\boldsymbol{x}$ with t_u^{-2} and mean energy $\mathcal{E} = (0.5/\mathcal{V}) \int_{\mathcal{V}} \boldsymbol{u}(\boldsymbol{x}) \cdot \boldsymbol{u}(\boldsymbol{x})\, \mathrm{d}\boldsymbol{x}$ with $\Gamma\nu/R_c^2$. Notably, we show the total helicity (rather than the mean value as with energy and enstrophy), because the normalized $\mathcal{H}$ is equal to 2, and we can directly compare with the vortex-dynamical results.

Due to the dissipative nature of the flow, there is monotonic energy decay (figure 5*a*). Similar to the vortex-dynamical case, Biot–Savart interactions induce a stretched structure of antiparallel vortices (figure 6*a–d*). This process intensifies enstrophy (figure 5*b*), and sustains energy and helicity dissipation rates (figure 5*a*,*c*). At time $t = 0.186$ (figure 6*e*), the system has proceeded beyond the enstrophy maximum; hence, the stretching process has concluded and the antiparallel vortex tubes comprising the stretched structure are in the process of annihilating each other via viscous diffusion. By time $t = 29$ (figure 6*f*), the original link has disappeared, yet, despite the unlinking process, the system retains 70 % of its initial helicity (figure 5*c*). This is because there is now a significant amount of *Tw* and *Wr* in the system. Indeed, there is evidence of core torsion at the chosen isosurface level of $|\boldsymbol{\omega}| = 154.4$ (figure 6*e*). Overall, there is agreement with the inviscid, vortex-dynamics results on *Lk* transformation into other topological helicity measures. The Navier–Stokes calculation brings forward the merits of the vortex-dynamical approach, since it is tube discretization into elementary vortices, which are tracked in time, that enables the unambiguous computation of topological helicity measures in that case.

Due to computational complexity of the Navier–Stokes $\hat{\mathcal{H}}(k)$ formula, we present lower-resolution (64^3) spectra (figure 7). Based on the expected inverse helicity cascade, this is not a true limitation. Since the Reynolds number is not very large, some effects of viscous dissipation on helicity physics are anticipated. The initial stages resemble the vortex-dynamical case (figure 7*a*). The spectral fluctuations are damped out, whilst the total helicity does not vary significantly. Similar to the inviscid case, there is a transition from alternating-sign helicity at different scales to exclusively positive values. At larger

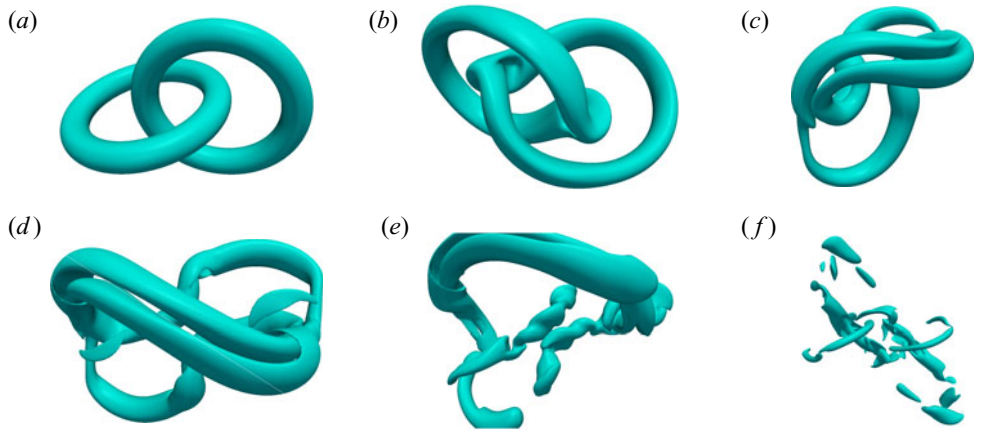

Figure 6. Vorticity magnitude isosurfaces at level $|\boldsymbol{\omega}| = 154.4$. From (a) to (f) the times are: 0, 0.05, 0.1, 0.14, 0.186 and 0.29.

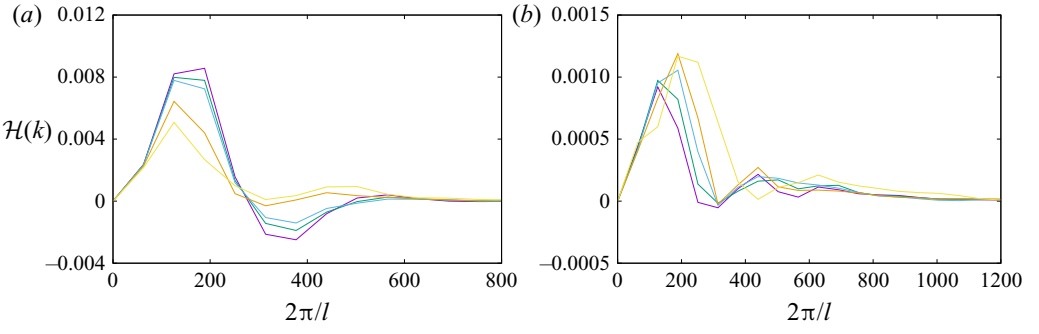

Figure 7. Navier–Stokes calculation. (a) Pre-enstrophy peak helicity spectra $\hat{\mathcal{H}}(k)$ at times $t = 0$, $t = 0.025$, $t = 0.037$, $t = 0.075$ and $t = 0.1$ (t_u units). Smaller times correspond to curves with higher peaks at small wavenumbers. (b) Post-enstrophy peak helicity spectra $\hat{\mathcal{H}}(k)$ at times $t = 0.302$, $t = 0.523$, $t = 0.586$, $t = 0.636$ and $t = 0.686$ (t_u units). Larger times correspond to curves with peaks at smaller wavenumbers.

times (figure 7*b*), the inverse cascade of the inviscid case is present in an incomplete way. Indeed, there is a shift of spectral peaks towards low wavenumbers, but since helicity is not conserved, and in contrast with the vortex-dynamics case, the peak levels are decaying instead of increasing. Hence, it was the inviscid nature of our vortex-dynamical system that enabled the unambiguous demonstration of the inverse helicity cascade. This was achieved with a low computational complexity calculation, that required significantly smaller processing and memory capacities than the Navier–Stokes computation.

6. Conclusion

Vortex links are destroyed by reconnections which are facilitated by viscous diffusion that allows vortex lines to slip past each other. A byproduct of this process is the dissipation of energy and helicity. The energy sink is equal to $-\int_{\mathcal{V}} \epsilon_e \, \mathrm{d}\boldsymbol{x}$, with $\epsilon_e = 2\nu S_{ij} S_{ij}$ which for an unbounded system becomes $\epsilon_e = \nu \boldsymbol{\omega} \cdot \boldsymbol{\omega}$, whilst the helicity sink is $-\int_{\mathcal{V}} \epsilon_h \, \mathrm{d}\boldsymbol{x}$, with $\epsilon_h = 2\nu \boldsymbol{\omega} \cdot \boldsymbol{\nabla} \times \boldsymbol{\omega}$. Since, as discussed in § 1, the conservation of helicity involves the vector product of velocity with frozen in the flow vector fields, it is reasonable

to associate helicity dissipation with the diffusion of the same vector fields (here the vorticity) enabled by viscosity (Layton 2007). Notably, the sink of streamline helicity is the vortex-line helicity (times ν for dimensional book-keeping). During reconnection, vortices are stretched, so both enstrophy and ϵ_e are intensified. The helicity sink has a different structure, but it too leads to a reduction of helicity. Our research suggests that disconnecting the reconnection phenomenon from its underlying physical mechanism (e.g. viscous dissipation in classical fluids, quantum stress action in quantum fluids or scissors and glue in Christmas ribbons (Pfister & Gekelman 1990)) can help understand better the experiments of Scheeler *et al.* (2014). Indeed, the purely topological act of reconnection conserves helicity (even if it destroys *Lk*) (Pfister & Gekelman 1990). On the other hand, the physical means by which reconnection is achieved could destroy some helicity as a byproduct of their action, but this ought not obfuscate the helicity-preserving nature of topological change. For example, in the classical fluid dynamics case, the short duration of high-Reynolds-number reconnection means that topological change can be achieved with small helicity destruction (since viscous dissipation does not have sufficient time to effect a sizeable reduction). Our calculations support these conclusions in two different ways: (*a*) by constructing, via the vortex-dynamics model of non-dissipative reconnections, a direct vortex analogue of the purely topological case of Pfister & Gekelman (1990), and indicating that helicity tends to be preserved in this case, and (*b*) by solving the Navier–Stokes equations for a smaller Reynolds number, demonstrating that viscous reduction of helicity is just a secondary side effect of the reconnection process, which conceals the fundamental helicity-preserving nature of topological reconnections. This concealment becomes more and more feeble as the Reynolds number increases, until, in our idealized vortex-dynamical computation, it becomes negligible as we reach the limit of purely topological change.

Our calculation indicates a transformation of pre-reconnection *Lk* to post-reconnection *Wr*. In this way, it is in full agreement with the experimental results of Scheeler *et al.* (2014). Interestingly, the constant pre-reconnection *Lk* values correspond to significant helicity spectrum dynamics, which conserve (in the inviscid limit) topology whilst eliminating small-scale helicity. The inverse helicity cascade computed here differs from the direct helicity cascade reported in the statistics of homogeneous, isotropic turbulence (Biferale, Musacchio & Toschi 2013). To understand this result better, we note that the computed helicity spectrum of a link composed of single line vortices shows (progressively decaying) fast, sign-changing variations at all scales. Similar in origin to energy spectrum ringing in vortex rings, these fluctuations are due to the potential flow around the line vortices, since they are eliminated at subcore length scales, when we replace lines with tubes. Similar helicity spectrum oscillations were observed for two perpendicular thin slabs of magnetic flux (Asgari-Targhi & Berger 2009). The key observation here is that, at every finite-scale interval, there is only a small net amount of helicity, as compared with the actual fluctuation amplitude. This is because there is a gradual reduction of the amplitude as we move towards smaller scales. These remarkable small-scale variations in the spectrum are directly related to the perfect-circle geometry of line vortices, and they disappear once the rings are deformed by Biot–Savart effects on the route to reconnection. However, since helicity is conserved, and the small-scale helicity associated with the perfect-circle geometry is destroyed as the rings become non-circular, the small-scale helicity needs to be transferred to larger scales. More concisely, small-scale helicity is associated with perfect-circle geometry and very small vortex cores, and as the geometry is altered on the route to reconnection whilst global helicity is conserved, the only physically viable process is for helicity to accumulate at large scales. The post-reconnection inverse

helicity cascade has possibly important implications for the structure of turbulence. Indeed, the magnification of $\boldsymbol{u}\cdot\boldsymbol{\omega}$ at large scales implies the weakening of the Lamb force $\boldsymbol{u}\times\boldsymbol{\omega}$, which is responsible for the nonlinearity of turbulence and the turbulence cascade. Perhaps some turbulent coherent structures are the remnants of reconnection-induced destructions of linked vortex rings. Thus, the post-reconnection dynamics could be associated with the formation of turbulent coherent structures and the inhibition of the direct energy cascade.

This work could be continued along various directions. It would be interesting, for example, to investigate the topological and helicity dynamics of magnetohydrodynamic vortex links. Such studies would significantly expand previous vortex-dynamical magnetohydrodynamic investigations (Kivotides 2018*a*, 2019). Another important problem is the topological and helicity dynamics of vortex knots, and possible connections between topology and energy and helicity spectra there, in conjunction with advanced topological measures including knot polynomials (Liu & Ricca 2015; Cooper *et al.* 2019) and Vassiliev invariants.

Declaration of interests. The authors report no conflict of interest.

Author ORCIDs.
Demosthenes Kivotides http://orcid.org/0000-0001-5619-0534.

References

Araki, K. 2015 Helicity-based particle-relabelling operator and normal mode expansion of the dissipationless incompressible Hall magnetohydrodynamics. *Phys. Rev.* E **92**, 063106.

Araki, K. 2018 Particle relabeling symmetry, generalized vorticity, and normal-mode expansion of ideal, incompressible fluids and plasmas in three-dimensional space. arXiv:1601.05477v2 [nlin.CD].

Aref, H. & Zawadski, I. 1991 Linking of vortex lines. *Nature* **354**, 50–53.

Asgari-Targhi, M. & Berger, M.A. 2009 Writhe in the stretch-twist-fold dynamo. *Geophys. Astrophys. Fluid Dyn.* **103**, 69–87.

Berger, M. & Prior, C.B. 2006 The writhe of open and closed curves. *J. Phys. A: Math. Gen.* **39**, 8321–8348.

Biferale, L., Musacchio, S. & Toschi, F. 2013 Split energy-helicity cascades in three-dimensional homogeneous and isotropic turbulence. *J. Fluid Mech.* **730**, 309–327.

Brady, M., Leonard, A. & Pullin, D.I. 1998 Regularized vortex sheet evolution in three dimensions. *J. Comput. Phys.* **146**, 520–545.

Călugăreanu, G. 1961 Sur les classes d'isotopie des noeuds tridimensionnels et leurs invariants. *Czech. Maths J.* **11**, 588–625.

Cooper, R.G., Mesgarnezhad, M., Baggaley, A.W. & Barenghi, C.F. 2019 Knot spectrum of turbulence. *Sci. Rep.* **9**, 10545.

Feynman, R. 1955 Application of quantum mechanics to liquid helium. *Prog. Low Temp. Phys.* **1**, 17–53.

Fukumoto, Y. 2008 A unified view of topological invariants of fluid flows. *Topologica* **1**, 003.

Galantucci, L., Baggaley, A.W., Parker, N.G. & Barenghi, C.F. 2019 Crossover from interaction to driven regimes in quantum vortex reconnections. *Proc. Natl Acad. Sci. USA* **116**, 12204.

Hänninen, R., Hietale, N. & Salman, H. 2016 Helicity within the vortex filament model. *Sci. Rep.* **6**, 37571.

Kambe, T. 2007 *Elementary Fluid Mechanics*. World Scientific Publishing.

Kedia, H., Kleckner, D., Scheeler, M.W. & Irvine, W.T.M. 2018 Helicity in superfluids: existence and the classical limit. *Phys. Rev. Fluids* **3**, 104702.

Kivotides, D. 2014 Energy spectra of finite temperature superfluid helium-4 turbulence. *Phys. Fluids* **26**, 105105.

Kivotides, D. 2018*a* Interactions between vortex tubes and magnetic-flux rings at high kinetic and magnetic Reynolds numbers. *Phys. Rev. Fluids* **3**, 033701.

Kivotides, D. 2018*b* Superfluid helium-4 hydrodynamics with discrete topological defects. *Phys. Rev. Fluids* **3**, 104701.

KIVOTIDES, D. 2019 Interactions between vortex and magnetic rings at high kinetic and magnetic Reynolds numbers. *Phys. Lett.* A **383**, 1601–1606.

KIVOTIDES, D., BARENGHI, C.F., MEE, A.J. & SERGEEV, Y.A. 2007*a* Interaction of solid particles with a tangle of vortex filaments in a viscous fluid. *Phys. Rev. Lett.* **99**, 074501.

KIVOTIDES, D. & LEONARD, A. 2003*a* Computational model of vortex reconnection. *Europhys. Lett.* **63**, 354–360.

KIVOTIDES, D. & LEONARD, A. 2003*b* Quantized turbulence physics. *Phys. Rev. Lett.* **90**, 234503.

KIVOTIDES, D. & LEONARD, A. 2004*a* Stringy turbulence kinematics. *Europhys. Lett.* **65**, 344.

KIVOTIDES, D. & LEONARD, A. 2004*b* Geometrical physics of the many vortex filament problem. *Europhys. Lett.* **66**, 69.

KIVOTIDES, D., MEE, A.J. & BARENGHI, C.F. 2007*b* Magnetic field generation by coherent turbulence structures. *New J. Phys.* **9**, 291.

KLENIN, K. & LANGOWSKI, J. 2000 Computation of writhe in modeling of supercoiled DNA. *Biopolymers* **54**, 307–317.

KNIO, O.M. & GHONIEM, A.F. 1990 Numerical study of a three-dimensional vortex method. *J. Comput. Phys.* **86**, 75–106.

LAYTON, W. 2007 Bounds on energy and helicity dissipation rates of approximate deconvolution models of turbulence. *SIAM J. Maths Anal.* **39**, 916–931.

LEGGET, A.J. 2006 *Quantum Liquids: Bose Condensation and Cooper Pairing in Condensed-Matter Systems*. Oxford University Press.

LEONARD, A. 1985 Computing three-dimensional incompressible flows with vortex elements. *Annu. Rev. Fluid Mech.* **17**, 523–529.

LIU, X. & RICCA, R.L. 2015 On the derivation of the HOMFLYPT polynomial invariant for fluid knots. *J. Fluid Mech.* **773**, 34–48.

MOFFATT, H.K. 1969 The degree of knottedness of tangled vortex lines. *J. Fluid Mech.* **35**, 117–129.

MOFFATT, H.K. 2014 Helicity and singular structures in fluid dynamics. *Proc. Natl Acad. Sci. USA* **111**, 3663–3670.

MOFFATT, H.K. & RICCA, R.L. 1992 Helicity and the călugăreanu invariant. *Proc. R. Soc. Lond.* A **439**, 411–429.

MOSTOVOY, J., CHMUTOV, S. & DUZHIN, S. 2017 *Introduction to Vassiliev Knot Invariants*. Cambridge University Press.

PADHYE, N. & MORRISON, P.J. 1996 Fluid element relabeling symmetry. *Phys. Lett.* A **219**, 267–292.

PFISTER, H. & GEKELMAN, W. 1990 Demonstration of helicity conservation during magnetic reconnection using Christmas ribbons. *Am. J. Phys.* **59**, 497–502.

RICCA, R.L. & MOFFATT, H.K. 1992 The helicity of a knotted vortex filament. In *Topological Aspects of the Dynamics of Fluids and Plasmas* (ed. H.K. Moffatt, G.M. Zaslavsky, P. Comte & M. Tabor), pp. 225–236. Springer.

SCHEELER, M.W., KLECKNER, D., PROMENT, D., KINDLMANN, G.L. & IRVINE, W.T.M. 2014 Helicity conservation by flow across scales in reconnecting vortex links and knots. *Proc. Natl Acad. Sci. USA* **43**, 15350–15355.

SCHEELER, M.W., VAN REES, W.M., KEDIA, H., KLECKNER, D. & IRVINE, W.T.M. 2017 Complete measurement of helicity and its dynamics in vortex tubes. *Science* **357**, 487–491.

SCHWARZ, K.W. 1985 Three-dimensional vortex dynamics in superfluid ^{4}He: line-line and line-boundary interactions. *Phys. Rev.* B **31**, 5782–5804.

SCHWICHTENBERG, J. 2017 *Physics From Symmetry*. Springer International Publishing.

SOSSINSKY, J. 2004 *Knots: Mathematics with a Twist*. Harvard University Press.

WINCKELMANS, G.S. & LEONARD, A. 1993 Contributions to vortex particle methods for the computation of three-dimensional incompressible unsteady flows. *J. Comput. Phys.* **109**, 247–273.

ZUCCHER, S. & RICCA, R.I. 2015 Helicity conservation under quantum reconnection of vortex rings. *Phys. Rev.* E **92**, 061001.

ZUCCHER, S. & RICCA, R.I. 2017 Relaxation of twist helicity in the cascade process of linked quantum vortices. *Phys. Rev.* E **95**, 053109.